This document is the unedited Author's version of a Submitted Work that was subsequently accepted for publication in Langmuir, copyright © American Chemical Society after peer review. To access the final edited and published work see https://doi.org/10.1021/acs.langmuir.9b01215.

Structure and Dynamics of Confined Liquids – Challenges for a Novel X-Ray Surface Force Apparatus

Henning Weiss,[1] Hsiu-Wei Cheng,[2] Julian Mars,[3,1] Hailong Li,[1] Claudia Merola,[2] Frank Uwe Renner,[4] Veijo Honkimäki,[5] Markus Valtiner,[6,2,a)] and Markus Mezger[3,1,b)]

[1)] *Max Planck Institute for Polymer Research, Ackermannweg 10, 55128 Mainz, Germany*
[2)] *Institute of Applied Physics, Vienna Institute of Technology, Wiedner Hauptstrasse 8-10/E134, 1040 Wien, Austria*
[3)] *Institute of Physics, Johannes Gutenberg University Mainz, 55128 Mainz, Germany*
[4)] *Hasselt University, Institute for Materials Research, 3590 Diepenbeek, Belgium*
[5)] *ESRF-European Synchrotron Radiation Facility, Avenue des Martyrs 71, 38043 Grenoble Cedex 9, France*
[6)] *Max Planck Institute for Eisenforschung, Max-Planck-Strasse 1, 40237 Düsseldorf, Germany*

(Dated: 25 April 2019)

In nano-technology, the molecular-scale structure and dynamics of confined liquids increasingly gain relevance for the applications of tomorrow. Thus, a detailed knowledge of the structure of confined liquids on molecular length scales is of great interest for fundamental and applied sciences. To study confined structures under dynamic conditions, we constructed an in-situ X-ray surface force apparatus (X-SFA). This novel device can create a precisely controlled slit-pore confinement down to molecular dimensions by using a cylinder-on-flat geometry for the first time. Complementary structural information can be obtained by simultaneous force measurements and X-ray scattering experiments. The in-plane structure of liquids parallel to the slit-pore and density profiles perpendicular to the confining interfaces are studied by X-ray scattering and reflectivity. The normal load between the apposing interfaces can be modulated to study the structural dynamics of confined liquids. The confinement gap distance is tracked simultaneously with nanometer precision by analysing optical interference fringes of equal chromatic order. Relaxation processes can be studied by driving the system out of equilibrium by shear stress or compression/decompression cycles of the slit-pore. The capability of the new device is demonstrated on the liquid crystal 4'-octyl-4-cyano-biphenyl (8CB) in its smectic A (SmA) mesophase. Its molecular-scale structure and orientation confined in an approx. 100 nm slit-pore was studied under static and dynamic conditions.

Keywords: confined liquid | liquid crystal | X-ray scattering | X-ray reflectivity | surface forces

I. INTRODUCTION

Confined liquids play an important role in many technical applications and processes. For example, the dynamics of electrolytes in nanoscale confinement are relevant for the development of novel electric double layer capacitors[1,2] and electrochemical processes[3–5]. In heterogeneous catalysis, the performance of a reaction has been shown to be sensitive to the molecular scale liquid structure in a nano-porous material[6]. In particular for complex electrolytes with heterogeneities on the nanometer length scale[7–10], confinement can qualitatively alter structural properties. High speed printing and film deposition on nanoscopically rough surfaces depend on the wetting property of surfactants in small pores. Thus, a detailed knowledge of the structure of confined liquids on molecular length scales is of great interest for fundamental and applied sciences.

When confinement approaches the molecular dimensions of liquids, structural and dynamical properties can differ significantly from their bulk behaviour[11–13] (Figs. 1a to 1d). It has been shown that, depending on the inter-molecular forces, liquids adjacent to a solid can exhibit interfacial regions of reduced density[14,15], interfacial freezing[16,17], or molecular layering[18–23]. Furthermore, the phase diagram of confined liquids can differ significantly from bulk[24,25]. Such interface induced structures can strongly affect the dynamics in a confined system. Prominent examples include increasing friction under lateral shear[26,27] as well as an increased reactivity at electrified interfaces[5] (Figs. 1e and 1f).

By today, most structural information on the molecular scale arrangement of confined fluids is obtained by computer simulations[30,31] or indirectly deduced from

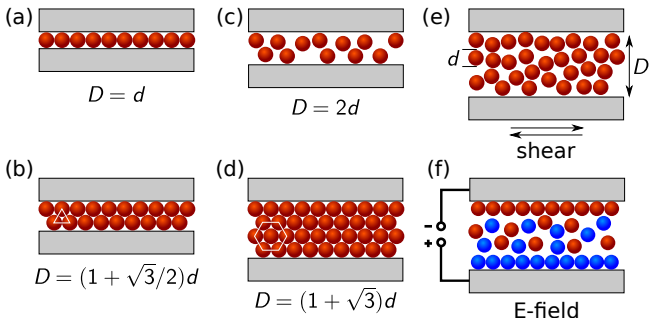

FIG. 1. Structure of hard spheres with diameter d in slit-pore confinement at a gap width $D = d$ (a), $D = (1 + \sqrt{3}/2)d$ (b), $D = 2d$ (c), $D = (1 + \sqrt{3})d$ (d). Dynamic response of the system after applying shear stress (e) or electric potential (f).

[a)] Electronic mail: valtiner@iap.tuwien.ac.at
[b)] Electronic mail: mezger@mpip-mainz.mpg.de

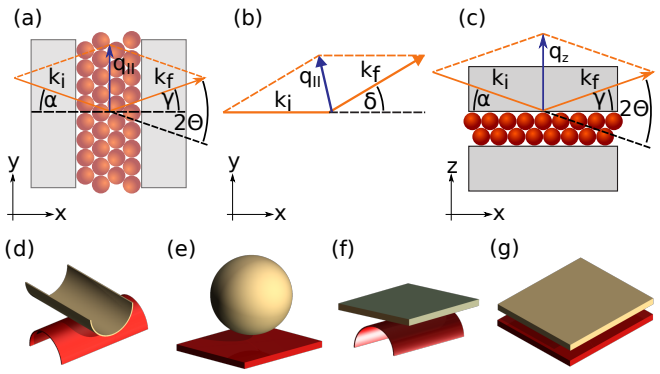

FIG. 2. Overview of X-SFA geometries to study confined liquids by X-ray scattering. Scattering angles follow the 6-circle notation by Vlieg et al.[28] with incident angle α, exit angle γ, in-plane angle δ, total scattering angle 2θ. (a) In transmission geometry, incident and scattered X-ray beams (orange) penetrate both confining slit-pore walls (grey)[29]. (b) In in-plane scattering geometry, the incident beam $\alpha = 0$ is aligned parallel to the confining surfaces. At $\gamma = 0$, the momentum transfer of the scattering vector $q = k_f - k_i$ points in the direction perpendicular to the surface normal, i.e. $q_{||}$ in the xy-plane. (c) Specular reflectivity with $\alpha = \gamma$ and $q = q_z$ parallel to the surface normal of the slit-pore walls. This configuration probes interfacial profiles along the z-direction, i.e. across the slit-pore. Confinement can be created in the standard SFA crossed cylinders geometry (d), the colloidal probe sphere-on-flat geometry (e), the cylinder-on-flat geometry (f), or the plane-plane geometry (g).

force-distance curves measured using a surface force apparatus (SFA, Fig. 2d), colloidal probe (Fig. 2e), or atomic force microscopy (AFM). In particular, the SFA is an established experimental setup to simultaneously measure forces and distances across two surfaces approaching each other on a range from micrometers down to nanometers with nanometer precision.

The paper is structured as follows: In Sec. II we give an overview over past and present experimental approaches to address molecular scale structures and dynamics of confined fluids by elastic scattering and force measurements. We then describe a novel design for an X-ray surface force apparatus (X-SFA) in cylinder-on-flat geometry combining the capabilities of a SFA setup with X-ray scattering techniques (Sec. III). In Sec. IV, we show first proof of principle experiments on the smectic liquid crystal 4'-octyl-4-cyano-biphenyl (8CB) in confinement. Our results demonstrate the feasibility of the cylinder-on-flat geometry and the increased sensitivity and capability of the new instrument. The paper closes with an outlook (Sec. V) where we discuss the potential of the new setup to answer current scientific questions in the field of soft condensed matter, develop ideas for future instruments, and outline first concepts for experiments that will become possible at new upcoming synchrotron sources[32,33].

II. EXPERIMENTS PROBING STRUCTURE AND DYNAMICS OF CONFINED LIQUIDS

The SFA is used to study liquids under controlled slit-pore confinement with gap dimensions on the molecular length scale[34]. Furthermore, a SFA can very precisely apply stress on the confined material and measure its viscoelastic response. However, the force measurements in a SFA, colloidal probe, or AFM, actually do not directly probe the spatial arrangement of the molecules[35,36]. Instead, structural information are extracted from force measurements using model assumptions to interpret the force data[37,38]. On the other hand, X-ray scattering and reflectivity (XRR) are powerful techniques to directly probe structures on molecular length scales in bulk and at interfaces[39–41]. Today, high-brilliant synchrotron sources allow to study the structural dynamics at interfaces and in small sample volumes in-situ on sub-microsecond time scales[42–45].

For instance, extensive work has been conducted on the molecular scale structure of soft matter confinement in porous bulk-like materials using X-ray and neutron scattering techniques[25,46–50]. Today, nearly mono-disperse cylinders in silica or aluminum oxide (AAO) with diameters ranging from 5 nm to 1 μm are available[51–55]. The macroscopic amount of liquid confined inside millions of uniform pores allows the use of bulk techniques such as dielectric spectroscopy[56,57], NMR[58], optical birefringent[25], or QENS[59]. However, even for such well defined pores, in scattering experiments structural information on the confined liquids is lost due to the intrinsic cylinder symmetry. In disordered and polydisperse porous materials, a quantitative interpretation of scattering data is even more challenging. Due to the Gibbs-Thomson effect[60–62], the large curvature in nano-sized porous materials strongly affects the phase behaviour of confined fluids[63]. Moreover, dynamic studies during shear, compression, and decompression are intrinsically difficult to realise experimentally in a porous system. Therefore, to probe the intrinsic structure and dynamics of liquids confined between two parallel walls, other geometries have to be employed.

An X-ray surface force apparatus (X-SFA) simultaneously combines the two complementary experimental techniques of force-distance measurements and X-ray scattering[34]. This unique combination promises results not accessible by any other experimental method. Moreover, a SFA allows moving the pore walls vertically and laterally with respect to each other. Therefore, the development of an X-SFA, that allows to drive the structure of the confined liquid out of equilibrium by lateral and vertical motion of the pore walls while recording its relaxation by scattering techniques will open up new ways to study the structural relaxation dynamics of confined liquids under shear and load.

The first X-SFA for transmission experiments (Fig. 2a) in crossed cylinder geometry (Fig. 2d) was introduced in 1993 by the groups of J. Israelachvili and

C. Safinya[26,64–69]. Experiments on the liquid crystal 4'-octyl-4-cyano-biphenyl (8CB) demonstrated, that a 10 nm thick 8CB film provides sufficient scattered intensity to extract structural information on the molecular orientation induced by the confinement between the two mica cylinders.

Later, two different teams, lead by H. Reichert and F. Mugele at ID10C[70], ESRF and J.F. van der Veen and M. Heuberger at the Swiss Light Source[71], used a similar geometry. The latter team also explored the potential of an X-SFA for X-ray reflectivity (Fig. 2c) using the crossed cylinder geometry (Fig. 2d)[72–75]. However, due to the large curvature of the cylinders, data can only be taken at large vertical momentum transfers $q_z > 4.0\,\mathrm{nm}^{-1}$. This precludes conventional XRR measurements. Therefore, the structure of the confined liquid can only be deduced from crystal truncation rods (CTR) using a rather complex data analysis[75]. No structural in-plane information (Fig. 2b) is accessible in this geometry, since a defined slit-pore confinement is only established at the very center of the crossed cylinders.

Later, the group of O. Seeck at PETRA III designed two different X-SFAs in plane-plane geometry (Fig. 2g)[76,77]. In their current version, confining walls are made of two diamond single crystals commonly used for diamond anvil cells. With a maximum possible force of 100 N applied onto the 200 μm diameter diamond culets in crystallographic (100) direction, pressures up to 3 GPa can be reached to obtain molecular-scale confinement. Parallel alignment of the apposing macroscopic planar interfaces can be rather challenging. Furthermore, in some cases the information extracted from the scattering patterns is limited by the diamonds surface roughness of approx. 1 nm rms and up to 1.4 nm peak-to-valley. In X-ray scattering and specular reflectivity experiments on confined liquid benzene, a gap thickness down to 5 nm was reached[77]. In an experiment on carbon tetrachloride crystal-liquid coexistence was found in slit-pore confinement[78]

Recently, a device enabling shear measurements while performing X-ray experiments were realised by the group of Kurihara[79]. Using a crossed cylinder geometry, scattering experiments probe the molecular structure parallel to the two confining surfaces.

For neutron scattering experiments, devices usually feature large confined areas to accommodate large beam footprints. Sizes up to square centimetres might aggravate a reproducible and precise confinements over the entire area. Particles trapped in confinement are prone to corrupt measurements. The larger the confined areas the more challenging is the elimination of contaminants.

The group of T. Kuhl succeeded in creating a 100 nm slit-pore confinement with ±15 nm local deviations[80,81]. Their cell allows shear experiments in the frequency range between 0.001 Hz and 20 Hz. This setup was primarily used to investigated confined polymer films[82].

Another instrument to study the structure of confined soft matter films upon applying a controlled external pressure using neutron reflectometry was developed by de Vos *et al.*[83]. Here, confinement down to the nanometer level and over large areas is achieved by an inflatable flexible membrane approach. With this approach they probed the effects of confinement on a poly(vinyl pyrrolidon) gel layer in water, a polyelectrolyte multilayer in water, and the lamellar structures of a D_2O swollen stack of supported lipid-bilayers. Over the last years, it has been demonstrated that this setup can provide detailed insights into the equilibrium structure of confined soft matter at known confining pressures. Various studies on polyelectrolyte brushes and lipid bilayers[84–87] have been reported. However, the instrument does not allow for lateral motion of the confining surfaces against each other.

Changes on the interfacial profiles of hexadecane under shear rates up to 1000 Hz have been studied by neutron reflectivity in a cone-plate rheometer[88–90]. An alternative setup at P10, PETRA III using a modified plate-plate rheometer was employed to study the influence of shear forces on the structure of bulk liquids by X-ray scattering techniques[91,92]. However, due to their large sample thicknesses most instruments based on conventional rheometers are not able to reach high enough shear rates to detect fast interfacial relaxation processes on the molecular length scale such as adsorption and desorption[93,94].

In Sec. III we present a novel design for an X-SFA in cylinder-on-flat geometry (Fig. 2f) for in-plane scattering (Fig. 2b) and specular XRR (Fig. 2c). Using white light interferometry, this device can realise a controlled confinement in slit-pore geometry with gap thicknesses D ranging from several 10 μm down to molecular length scales. With this set-up, we can precisely control the thickness of the confined liquid, probed by the X-ray beam, over lateral areas up to $l \approx 5$ mm along the cylinder apex and $w \approx 80\,\mu$m width. The instrument is capable to apply lateral (shear stress) and vertical (compression/decompression) relative motion of the confining solids and monitor structural changes in-situ. Simultaneously, normal and frictional forces can be measured by strain gauges. Thus, X-SFA experiments can provide complementary information to force distance measurements and conventional X-ray and neutron scattering studies in nano-porous materials.

III. X-RAY SURFACE FORCE APPARATUS

A. General Design

In our new X-SFA setup (Fig. 3 and 4), confinement is realised between a stationary upper planar surface and a cylindrically curved lower surface in a flat-on-cylinder geometry (Fig. 2f). Both surfaces in direct contact with the liquid are atomically smooth with a roughnesses below 0.5 nm rms (Fig. S2). Their surface properties can be tuned by functionalisation with self assembled monolayers (SAMs).

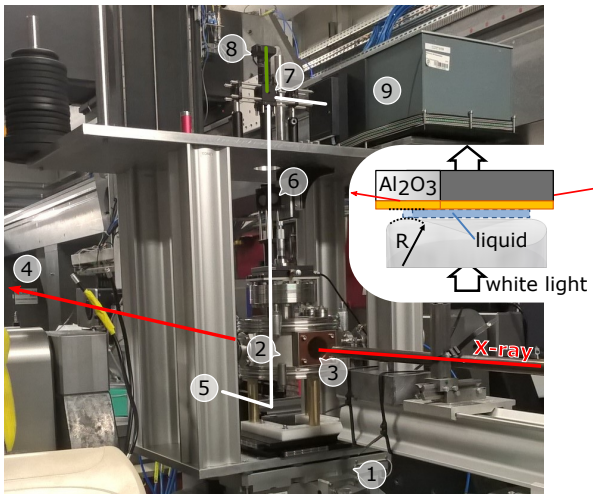

FIG. 3. Photography of the X-SFA setup mounted on the HEMD diffractometer (1) at ID31 ESRF. Lines indicate optical (white and green light) and X-ray (red) beam paths. The SFA with the confined liquid (inset) is located at the diffractometers rotation center inside a helium-filled stainless steel chamber (2). X-rays enter and leave the chamber nearly horizontally through 80 μm Kapton windows (3) and are recorded on 2D-detectors (4). White light from a fibre light source (5) is fed in via a mirror from below. Microscope objective (6), beam splitter (7), top view CCD camera (8), and spectrometer (9) are mounted above the sample chamber on the upper instrument level.

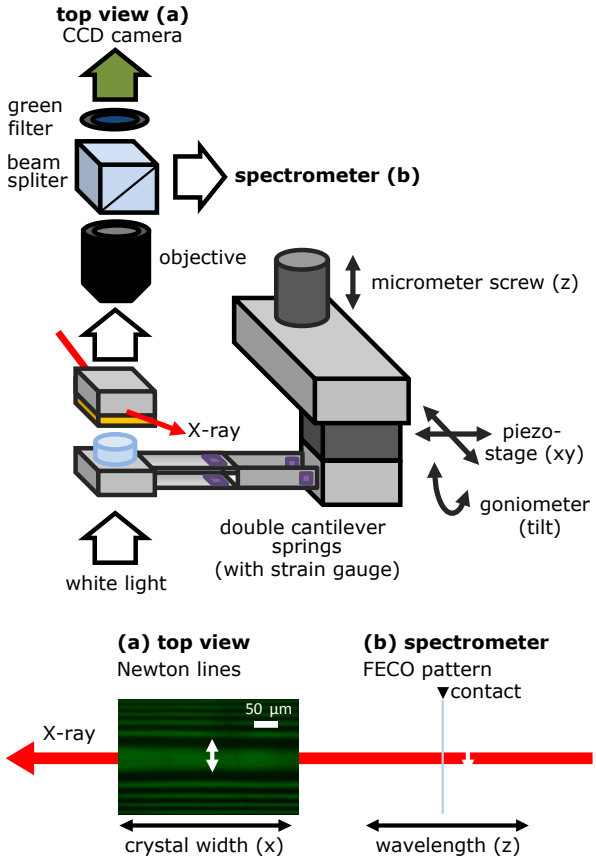

FIG. 4. Schematic of the X-SFA setup including double cantilever springs with strain gauges and optics for recording Newton's interference and fringes of equal chromatic order (FECO). (a) Top-view of the confined 8CB by video microscopy indicating perfect parallel alignment of the apposing surfaces. (b) FECOs are used to determine the gap width.

As stationary surface we use an atomically smooth template stripped gold layer on a corundum (Al_2O_3) single crystal (Fig. S1)[95–98]. A thin mica sheet, back coated with a semitransparent silver mirror serves as non-stationary (moving horizontal/lateral) surface. For mechanical support, the mica sheet is glued on a glass cylinder by epoxy resin. Preparation procedures and materials parameters for both surfaces are provided in the SI.

The incident X-ray beam enters through the side of the upper substrate in direction of the cylinder apex. This avoids scattering artefacts from the mica edges. The Al_2O_3 single crystal reduces background scattering from the substrate. Since in reflection geometry the beam has to penetrate through several millimetres of Al_2O_3, high energy X-rays are essential[99–101].

Due to the elasticity of the hardened epoxy resin, the mica sheet can comply with the planar non-stationary surface when pressed against each other. This generates a slit-pore with length $l = 4.8$ mm defined by the crystal size, and width $w \sim 100\,\mu$m depending on the applied pressure. Thus, the cylinder-on-flat geometry provides a confined area, much larger than for conventional crossed cylinder setups (Fig. 2d). For a slit-pore gap width $D = 2\,\mu$m, length $l = 5$ mm and width $w \sim 100\,\mu$m, at sufficiently small incident angles α_i a sample volume of 10^{-3} mm^3 can be illuminated by the X-ray beam. This volume is about 10 - 50 times lager compared to other X-SFA setups in reflection geometry[73,77], with the caveat of difficult alignment.

The SFA is mounted inside of a cylindrical gas tight stainless steel chamber (Fig. 3). A helium atmosphere improves thermal stability of the setup and reduces background scattering. The relative humidity (r.h.) inside the chamber can be controlled between $0\% - 90\% \pm 3\%$ by a humidifier inserted in the helium stream, constantly purging the chamber.

Alignment of the nanometer confinement is measured and controlled using an interference microscope based on multiple beam white light interferometry (Fig. 4b). Alignment of a cylinder-on-flat geometry requires additional degrees of freedom for rotating the apex of the cylinder in parallel with the flat surface. Therefore, a goniometer is used to align the cylindrical disc in parallel with the crystal surface. Successful alignment is characterised by Newtons lines that can be visualised in the transmitted beam (Fig. 4a). To achieve such an alignment, mica surfaces have to be glued to the cylindrical support in such a way that they do not wrinkle over the entire confined zone of the apposing crystal. For this purpose mica surfaces are ideally 8 μm - 10 μm thick to

provide adequate stiffness.

For dynamic studies, the cylindrical surface can be moved normal and lateral against the planar stationary surface with nanometer precision using piezo-electric transducers. Horizontal sliding motion is aligned in the direction of the cylindrical contact, in order to maintain the confined zone within the same line of sight for the X-ray beam. Strain gauges are used for simultaneous recording forces in both lateral and normal direction. Figure S3 displays a typical force versus distance and force versus time characteristic recorded with the X-SFA in the slit-pore geometry. The maximum applied pressure is determined by the chosen combination of the piezo travel range, cantilever spring-constant, and the elasticity of the glue. This limits recording of constant-approach-rate force distance characteristics to approximately $D = 200$nm. Further confinement was achieved by manual motion with micrometer screws and contact-jogging with triangular-wave compressions (Sec. IV C), to a minimum distance of 110nm, or approximately $30 - 40$ layers of 8CB. For a highly viscous fluid such as water this would compare to about 7 nm confinement.

B. In-Situ X-Ray Scattering and Reflectivity

X-ray scattering experiments have been performed at the high energy beamline for buried interface structure and materials processing ID31 at ESRF-European Synchrotron Radiation Facility, Grenoble, France. Figure 5 shows a sketch of the beamline layout and X-ray optics. The X-ray beam from a cpmU22 undulator is parallelised by the first CRL transfocator (TF1)[102,103] and monochromised by two multilayer mirrors (MLM, energy 70.0 keV). A second CRL transfocator (TF2) focus the beam onto the sample position with a $5 \times 20\,\mu\text{m}^2$ spot size normal and parallel to the slit-pore, respectively. To minimise the radiation dose on the sample, a 7 stage absorber (Poly-(methylmethacrylate); PA) and fast shutter (FS) are used. For sample positioning and orientation, the X-SFA was mounted onto the High Energy Micro Diffractometer (HEMD) setup for surface and interface studies[100,101]. Scattered intensities are alternatively detected by two 2D hybride pixel detectors. High resolution and low background signal is achieved by the CdTe MAXIPIX system (256×256 pixels, $55\,\mu$m pixel size) mounted behind a collimation system (CS, DS). The Dectris PILATUS 3 X CdTe 2M detector (1478×1679 pixels, $172\,\mu$m pixel size), behind a beam stop (not shown) to absorb the primary and specular reflected beam, is mounted on a dolmen like granite construction[104].

To probe buried interfaces, the high energy X-ray beam impinges the slit-pore through the side of the corundum (Al_2O_3) single crystal (Fig. S1, length 4.8 mm, X-ray transmission 67.5%). Background scattering from the single crystalline substrates is primarily caused by Compton and thermal diffuse scattering and significantly reduced compared to amorphous materials. At the critical angle $q_c = 0.768\,\text{nm}^{-1}$ of gold the footprint on the substrate is 4.8 mm.

Density profiles perpendicular to the confining interfaces were investigated by X-ray reflectivity (XRR) (Fig. 2c). Scattering experiments with the momentum transfer q parallel to the slit-pore probe the in-plane structure of the confined liquid (Fig. 2b). Scattering angles were converted to momentum transfer using $q = {}^{4\pi}/_{\lambda}\sin(\theta)$.

IV. STRUCTURE AND DYNAMICS IN CONFINED 8CB

A. Smectic Liquid Crystal 8CB

As model system, we choose the liquid crystal (LC) 4'-octyl-4-cyano-biphenyl (8CB). At 22°C, 8CB exhibits a smectic A (SmA) phase (Fig. 6). 8CB is known to form dimers by π-π-stacking of adjacent phenyl rings. This leads to a dimer-molecule dimensions larger than a single 8CB molecule (Fig 6)[27]. The lamellar arrangement of the rod-like molecules in smectic layers gives rise to a pronounced scattering peak in the small angle scattering (SAXS) regime (Fig. 2b).

In 8CB, bulk measurements showed that shear stress induces alignment, reduction of defects, and initiates the growth of smectic grains[92]. For the shorter homologue 6CB, resonance shear measurements in confinement detected an increase of viscosity for $D < 20\,\text{nm}$[105]. Below 12.5 ± 1.3 nm, orientation of the confined molecules was so large and the rigidity so high that the LC structure could not be distorted by electric fields. Moreover, this system has been extensively studied using crossed cylinder X-SFAs in transmission geometry[64–66,106,107]. Therefore, the liquid crystal 8CB serves as ideal benchmark system to assess the capabilities of an X-SFA.

Here, aside from static XRR and in-plane scattering on the LC structure in slit-pore confinement, time resolved experiments were carried out during compression and decompression cycles. Furthermore, the recorded X-ray scattering and reflectivity data was complemented by simultaneous interferometry based thickness measurements. Therefore, in contrast to static X-SFA[106] and macroscopic dynamic experiments[92] our setup allows to directly address the structural relaxation dynamics of the confined LC. To study confined structures over a wide gap range, data was taken at $D = 1700\,\text{nm}$ and 120 nm gap width. For a defined orientation of the 8CB molecules at the upper and lower interface, both confining surfaces were hydrophobised by self-assembled monolayers of hexadecane-thiol and octadecyl-trichlorosilane, respectively. From work by the Israelachvili group it is known that in such hydrophobised slit-pores the long axis of 8CB dimers are aligned parallel to the surface normal[27].

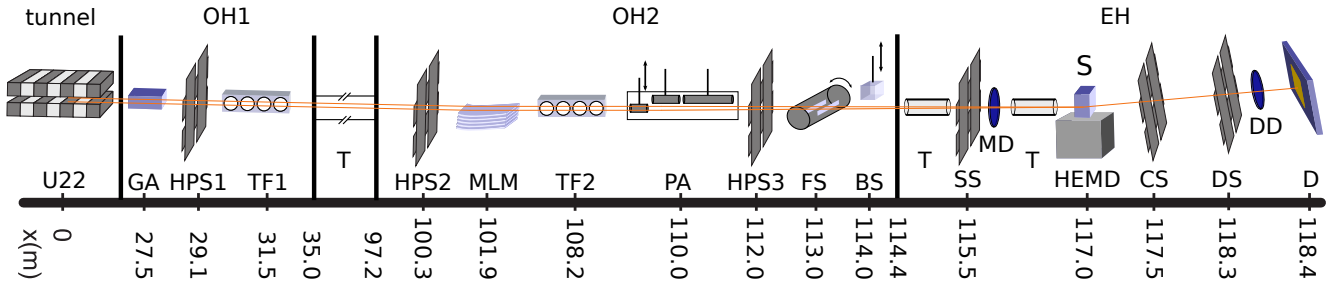

FIG. 5. (Color online) Beamline setup for high energy scattering experiments at ID31 ESRF (Feb. 2016): (OH1/2) optics hutches; (EH) experimental hutch; (U22) 22 mm periode permanent magnet in-vacuum undulator; (GA) gas absorber (1 m Argon at 300 mbar); (HPS1/2/3) high power slits; (TF1/2) compound refractive lens (CRL) transfocators; (MLM) horizontal multilayer double monochromator in fixed-exit geometry; (PA) PEEK (polyether ether ketone) absorber set; (FS) rotary fast shutter; (BS) beam safety shutter; (T) flight tubes; (SS) secondary slits; (MD) silicon PIN monitor diode; (HEMD) high-energy microdiffraction setup; (S) sample position; (CS) collimator slits; (DS) detector slits; (DD) silicon PIN detector diode; (D) 2D detector (CdTe MAXIPIX). Distances are not to scale.

B. Static Structure of 8CB in Confinement

Figure 7a shows in-plane scattering data at $D = 1700\,\text{nm}$. In in-plane scattering geometry, experiments recording $I(q_\parallel)$ with momentum transfer $q_\parallel = \sqrt{q_x^2 + q_y^2}$ are sensitive to the structure in the x-y-plane, i.e. parallel to the solid/liquid interface (Fig. 2b).

Qualitatively, the recorded data exhibits the characteristic scattering pattern of a LC in the SmA bulk phase[108,109]. The sharp diffraction peak (I) at $q_\text{I} = 2.0\,\text{nm}^{-1}$ corresponds to $^{2\pi}/_{q_\text{I}} = 3.1\,\text{nm}$ real space distance. This periodicity compares well to the periodicity of 3.2 nm for the SmA mesophase of 8CB confined in between two hydrophobised surfaces as observed in SFA experiments[27]. Therefore, it is assigned to the long axis of an 8CB dimer, defining the periodicity of the quasi long range ordered liquid crystalline smectic layers (Fig. 6). Around $q_\text{II} = 14\,\text{nm}^{-1}$ a second, broad diffuse peak (II) appears. Its 0.45 nm periodicity corresponds to the average lateral distance between neighbouring rod-like 8CB molecules within the same smectic layer. The large FWHM of $4\,\text{nm}^{-1}$ originates from the short range order perpendicular to the long axis of the 8CB dimers.

However, on the quantitative level remarkable differences with respect to non-textured bulk samples are observed. In bulk the integrated intensities of the sharp (I) and diffuse (II) peaks are on the same magnitude. In contrast, the recorded scattering pattern (Fig. 7a) shows a much larger area under peak II. This is a first indication that the director of the confined LC exhibits a preferred orientation parallel to the interface normal.

Specular reflectivity $I(q_z)$ probes the density profile perpendicular to the solid/liquid interface (Fig. 7b red curve). The critical angle of total reflection at $0.768\,\text{nm}^{-1}$ is given by the large scattering contrast between the gold mirror and the Al_2O_3 block. At higher q_z, the X-ray beam is transmitted into the gold layer and the slit-pore filled with 8CB. Kiessig fringes of period-

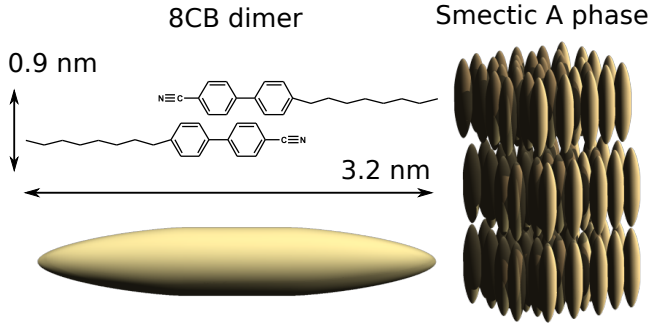

FIG. 6. Rod like structure of 4'-octyl-4-cyano-biphenyl (8CB) dimers (left) and molecular alignment of mesogens in the liquid crystalline smectic A phase (right).

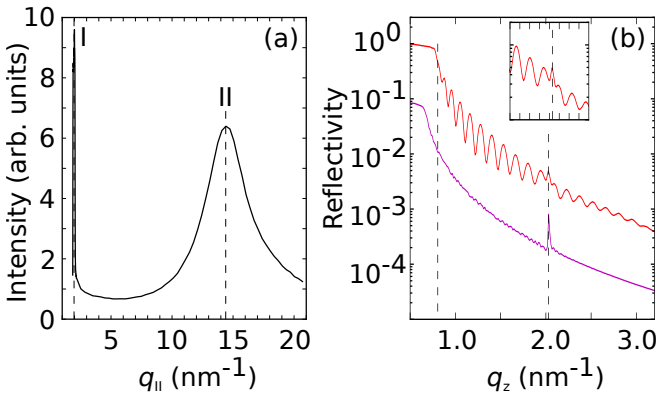

FIG. 7. Scattering signal from confined 8CB. (a) In-plane pattern $I(q_\parallel)$ recorded in the scattering geometry depicted in Fig. 2b. (b) Measured (red) specular X-ray reflectivity $R(q_z)$. Model calculated reflectivity curve (purple, vertically shifted by one order of magnitude) from a periodic arrangement of 560 smectic 8CB layers arranged with their long axis perpendicular to the solid/liquid interface.

icity $\Delta q = 0.15\,\mathrm{nm}^{-1}$ originate from interference at the 40 nm thick gold layer. At approximately $2\,\mathrm{nm}^{-1}$ a sharp Bragg-like peak is observed. Like observed for peak I, in in-plane scattering geometry (Fig. 7a), this reflection is attributed to the smectic order, i.e. the long-axis of 8CBs molecular pairs. For comparison, the purple curve in Fig. 7b shows a calculated XRR curve based on a simplified model consisting of 1700 nm 8CB, i.e. 560 smectic layers with 3.2 nm periodicity, adjacent to a semi infinite gold substrate.

Comparison with the in-plane scattering data (Fig. 7a) shows, that the integrated intensity found in specular condition, i.e. with the momentum transfer perpendicular to the solid/liquid interface (z-direction), is orders of magnitudes stronger than along $q_{\parallel}$. Likewise, 2D scattering data show a pronounced maximum in the specular direction (Fig. 8a and Fig. 8c). The observed angular intensity distribution over the scattering rings of constant total momentum transfer $q = \sqrt{q_{\parallel}^2 + q_z^2}$ originates from the confinement induced anisotropic orientation of the LC director. The observed scattering patterns indicate that the smectic 8CB layers are preferably arranged with their long axis perpendicular to the solid/liquid interfaces. This layered structure can now be stressed by compression and decompression exerted on the confined LC structure, by moving the lower mica cylinder in vertical direction (inset of Fig. 3).

C. Relaxation Dynamics

In the second part, we investigated the structural relaxation dynamics of confined 8CB that was brought out of equilibrium by periodic compression and decompression cycles. Changes in the gap width $D(t)$ are continuously monitored by the FECO interference pattern. Simultaneously, the structured arrangement of the 8CB molecules is probed in real-time using specular XRR or X-ray scattering.

For the first part of the experiments, the confining surface distance was set to $D = 1700\,\mathrm{nm}$. This corresponds to about 560 smectic layers of 8CB dimers (Fig. 6). Figure 8b shows the time evolution over two consecutive periodic compression/decompression cycles. A periodic trapezoidal signal with 8 s ramp time and 60 s holding time (period 136 s) was applied to the confined liquid. The top most black curve depicts the compression/decompression profile. Grey shaded areas indicate decompression, white areas compression. Recorded X-ray signals are shown in red, green and blue. The red curve corresponds to the specular XRR signal at $q_{\mathrm{I}} = 2.0\,\mathrm{nm}^{-1}$ with the momentum transfer pointing in z-direction (Fig. 7b, peak I). The green and blue curves describes the signal recorded in-plane (x-y plane, Fig. 7a) at a momentum transfer $q_{\mathrm{I}} = 2.0\,\mathrm{nm}^{-1}$ (peak I) and $q_{\mathrm{II}} = 14\,\mathrm{nm}^{-1}$ (peak II), respectively. All recorded signal intensities exhibit a strong time dependence, periodically

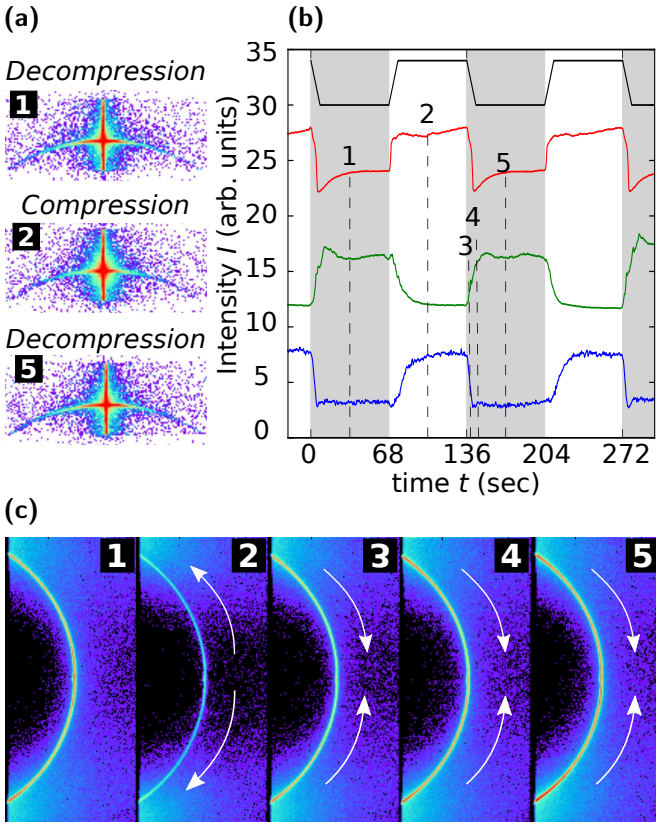

FIG. 8. (Color) Dynamic compression/decompression experiments at $D \approx 1700\,\mathrm{nm}$. (a) 2D pattern around specular condition. The arc is located at $q_{\mathrm{I}} = 2.0\,\mathrm{nm}^{-1}$. (b) Time evolution of compressive stress (black, 8 s ramp, 60 s holding time), specular XRR SmA first order signal (red, $q_{\mathrm{I}} = 2.0\,\mathrm{nm}^{-1}$, q_z-direction), in-plane scattering SmA first order signal (green, $q_{\mathrm{I}} = 2.0\,\mathrm{nm}^{-1}$, 90° rotated vs. red), in-plane scattering diffuse signal (blue, $q_{\mathrm{II}} = 14\,\mathrm{nm}^{-1}$, 90° rotated vs. red). Curves are scaled and vertically shifted for clarity. Grey areas indicate decompression, white areas pressure increase. (c) 2D pattern in in-plane direction. The arc is located at $q_{\mathrm{I}} = 2.0\,\mathrm{nm}^{-1}$. Areas in vertical scattering direction are masked to protect the detector from high intensities. Timestamps are numbered 1 to 5.

following the applied stress.

At $t = 0\,\mathrm{s}$ the confinement gap is opening. During the 8 s decompression interval the specular intensity drops by 46% (red curve). At the same time, the in-plane scattering intensity of peak I is increasing by a factor of 5 (green curve) whereas peak II is instantaneously decreasing by 17%. Upon subsequent compression ($t = 68\,\mathrm{s}$), the opposite behaviour is observed. While XRR and the in-plane peak II intensities are increasing, the in-plane peak I signal decreases. This proofes that upon compression/decompression the signal modulation is not dominated by the amount of 8CB inside the slit-pore. Instead, the scattered intensity is redistributed over rings of constant momentum transfer.

More insight on the redistribution of scattered intensities is obtained from the 2D scattering patterns. Figure 8

FIG. 9. (Color) Sketch of the molecular structure in 8CB after subsequent compression/decompression cycles. 8CB mesogens (red) entering the pore during decompression are miss-aligned with respect to the majority domain (brown). Upon compression, these molecules are more likely expelled from the slit-pore or pushed inside the majority domain leading to an overall increase of alignment.

shows a selection of detector images recorded around specular condition (b) and with the detector rotated in in-plane direction (c). During compression segments (timestamp 2) we observe a well focussed specular peak but only little intensity in the perpendicular in-plane direction. For decompression segments (timestamp 1 and 5), the situation is reversed. The specular peak becomes wider, stretching further over the diffraction ring. Accordingly, scattered intensity is redistributed towards off-specular directions where the signal is increasing. The intensity of the broad scattering peak II at $q_{\parallel} = 14\,\mathrm{nm}^{-1}$ in in-plane direction (blue curve), shows an inverse signal modulation. This is readily explained by the local anisotropy in the SmA phase of rod like mesogens. Here, the long period exhibiting quasi long range order (low-q, peak I) is oriented vertically. Perpendicular to this long axis, we have liquid-like short range order with shorter periodicity (high-q, peak II).

The observed redistribution of scattered intensity from the specular to the in-plane direction and vice versa indicates that the degree of orientational order is strongly affected by compression and decompression. Compression increases the overall alignment of the smectic layers parallel to the confining interfaces. 8CB dimers not aligned in preferred orientation with respect to the interfaces are more likely to be expelled from the slit-pore compared to those located within the majority domain.

During decompression new material is entering the slit-pore. At this moment, the extra material is not yet oriented by the interfaces (Fig. 9). In the pore center, mesogens leave the aligned majority domain to fill the extra space. This explains the strong 5 fold intensity increase of peak I in in-plane direction. At the same time, the new material is disturbing the existing aligned smectic structure. Thus, scattered the intensity becomes less focused in specular direction (Fig. 8a, timestamps 1 and 5), This leads to vertical streaks originating from the specular reflection along a ring of constant wave vector transfer. Accordingly, the specular intensity is decreasing.

Further information on the dynamics of structure formation is obtained from the relaxation of the scattering

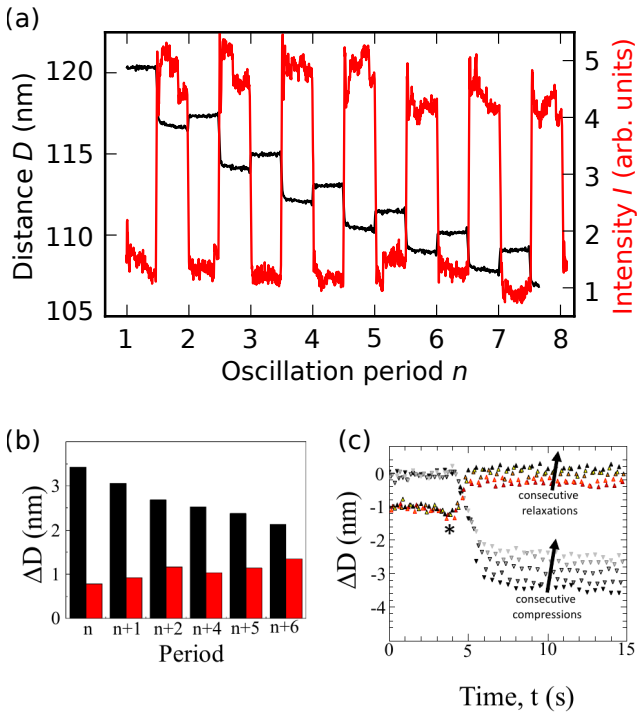

FIG. 10. (Color) Cyclic compression/decompression experiment at gap width $107\,\mathrm{nm} \leq D \leq 120\,\mathrm{nm}$ (2 s ramp, 30 s holding time). (a) Time evolution of gap distance (black) and specular XRR $I(q_z)$ (red) during compression/decompression cycles. Grey areas indicate decompression, white areas pressure increase. (b) Change in gap distance ΔD upon subsequent compression (black) and decompression (red) intervals. (c) Gap distance evolution over the first 15 s holding time.

signal compression and decompression. After decompression is completed, the specular intensity is gradually recovering (Fig. 8b, red curve, timestamps 1 and 5). With a relaxation timescale of approx. 20 s the signal is converging towards a plateau value during the 60 s holding time. However, a degree of orientational order comparable to what was observed after compression is not regained. Likewise, during compression clear relaxation processes on comparable time scales were observes for peak I and II in in-plan direction (Fig. 8b, green and blue curves, timestamp 2).

In the second part, we present results obtained for smaller gap sizes below 120 nm. This confinement gap amounts to an equivalent of less than 40 smectic 8CB layers. At this distance, the gap width can be precisely measured by FECO.

Fig. 10a shows the results from an XRR measurement (red curve) recored during periodic compression/decompression cycles. A trapezoidal force profile (amplitude 2 mN) with 2 s ramp time and 30 s holding time (period 64 s) was applied. Over 5 full compression/decompression cycles the gap distance (black curve) decreases by approx. 10 nm. As observed for the 1700 nm slit-pore, compression results in an increase of specular

XRR signal (white areas) while intensities decrease for decompression (grey areas).

During initial compression, the gap size collapses by about 3.4 nm. This distance is close to the dimension of 3.2 nm for the long axis of an 8CB dimer (peak I). However, during decompression the gap opens by only 0.8 nm. This value corresponds to the short axis of an 8CB dimer (peak II). Therefore, we conclude that during compression a single smectic 8CB layer is expelled from the slit-pore. During decompression mesogens with the long axis lying parallel to the confining surfaces emerge.

During subsequent compression events, the change in gap width decreases monotonously from 3.4 nm to approx. 2.0 nm (Fig. 10b). In contrast, during decompression the gap opening increases slightly to approx. 1.3 nm. Hence, the overall decrease in gap width detected during the experiment is decreasing with time.

We suggest that after sufficient cycles, during decompression horizontally aligned mesogens are periodically pulled out from aligned majority phase. Subsequently, they get pushed back during compression. A similar perpendicular orientation of mesogenes has been observed in simulations[110]. They belong to so called parking-lot-states that occur as transition states when rod-like LC mesogenes diffuse from one smectic layer to the other. For diffusion processes time scales are much faster. However, it is plausible that for confinement LCs under compressive stress similar structural process might take place.

For the small gap width of 120 nm, the lying down mesogens entering the pore upon decompression are trapped. During the 30 s holding time they can not align with the perpendicular oriented majority domain. Therefore, unlike for the 1700 nm pore, no clear relaxation processes indicating reorientation are observed by XRR. Likewise after the 2 s decompression ramp no more changes in gap thickness were detected during the subsequent 15 s holding time (Fig. 10c).

V. CONCLUSIONS AND OUTLOOK

A. The X-SFA with Cylinder-on-Flat Geometry

Over the last decades, several groups presented scientific instruments to investigate the molecular scale structure of fluids, confined inside a slit-pore, by X-ray and neutron scattering techniques. Reviewing the capabilities of the complementary designs (Sec. II), we motivate the need for an novel approach that allows to

- study the structure of soft matter in slit-pores parallel and perpendicular to the confining interfaces by specular XRR and X-ray scattering,
- control the slit-pore gap distance on the micrometer-to-nanometer length scale,
- simultaneously measure normal and tangential forces acting on the confining interfaces while recording X-ray scattering data,
- investigate the relaxation dynamics of a system that was brought out of equilibrium by compression/decompression or shear stress in time resolved experiments.

Based on geometry considerations we come up with with a novel X-SFA using a cylinder-on-flat geometry. This instrument can fulfil all the requirements outlined above in one single instrument. Compared to previous X-SFA designs, the cylinder-on-flat geometry allows to increase the amount of illuminated confined sample volume by more than one order of magnitude. Thus, the described instrument is no more limited to static measurements. In addition, time resolved scattering experiments with high temporal resolution become feasible. At the same time, the X-ray dose deposited on the sample is kept at an acceptable level.

The asset of the new X-SFA instrument are dynamic in-situ studies on the response of a confined liquid after an external stimulus. The system can be brought out of equilibrium by shear stress or compression and decompression of the slit-pore. Subsequently, structural relaxation dynamics are recorded by scattering techniques. At the same time, force and distance measurements provide complementary information on the dynamics of the system under sliding conditions[26,27,67].

The feasibility of the new X-SFA geometry was demonstrated by experiments on the smectic LC 8CB. The X-SFA can be employed to create and control slit-pore confinement while simultaneously determine the molecular scale structure of soft matter by X-ray scattering techniques. Furthermore, it allows to probe the structural relaxation dynamics of the confined LC mesophase under stress.

B. Scientific Research Directions

Possible fields for future studies include systems that exhibit anisotropic non-equilibrium structures that are induced by shear forces. Shear forces can induce orientation of confined liquids and modify their phase stability. For macromolecules, large anisotropic molecules, and LCs such effects are already well known[92,105]. However, compared to classical rheometers, a SFA can provide higher shear rates. This allows studies on confined liquids with lower viscosity and faster dynamics. Examples include water and short-chain alkanes where the influence of shear on the interfacial structure is still under debate[89,90,111].

Moreover, structure and dynamics of confined liquids play crucial roles in topics ranging from energy materials to environmental sciences. Examples include subjects related to spreading of surfactants, wetting dynamics, electrolytes in electric double layer capacitors and batteries,

the structure and dynamics of confined polymer melts. In nano-tribology open questions such as friction and the abrasive behaviour on the nano-meter length scale can be addressed[112].

A particular interesting research direction includes studies on confined complex electrolytes such as ionic liquids and complex solvent mixtures. These materials exhibit structural heterogeneities on the nanometer length scale[7,8,10,22,113]. At solid/liquid[19,114,115] and liquid/vapour interfaces[15,17,116,117] layered structures have been observed. Therefore it is anticipated that confinement can have strong influences on IL structures[118–120].

C. Future Instrument Developments

Aside from shear and normal forces (Fig. 1e), other stimuli can be employed to drive a confined system out of equilibrium. Examples include the application of an electrical potential (Fig. 1f). This allows to investigate the dynamics of interfacial hydration layers and adsorption and desorption of ions in solution. Another possibility are short light pulses. They can be used to rapidly increase temperature and studying phase transitions in confinement. Alternatively, light can be used to switch the conformation of molecules such as azobenzenes. Subsequently, the structural response of the confined system to conformational changes can be investigated.

With the upcoming upgrades of synchrotron radiation sources to diffraction limited storage rings[32,33] entirely new types of scattering experiments will become feasible. Currently, typical beam sizes for high-energy X-rays at PETRA III and ESRF are in the range of 10 μm horizontally and 5 μm vertically. After the ESRF EBS upgrade, the projected beam sized size at ID31 is 1 μm $\times$ 200 nm (horizontal $\times$ vertical) at a 15 times higher flux compared to today. For X-SFA experiments we foresee the potential for two important breakthroughs that are beyond current capabilities.

Currently, typical vertical beam sizes are compatible with the approx. 100 μm wide homogeneous slit-pores formed by pressing a flexible supported mica cylinder onto a rigid flat substrate. However, we anticipate that in the future hard materials SFA contacts between metals, semiconductors, and ceramics are also interesting probe system with high relevance in industrial applications. Due to their high elastic modulus, these materials cannot comply to the opposing flat surface. Therefore, it will be challenging to generate slit-pores with constant gap thicknesses, lateral extending over more than a few micrometers. Thus, smaller horizontal beam sized on the order of 1 μm will be highly beneficial to study realistic systems such as wet lubricants between hard matter surfaces.

Second, there is a large interest in the structure and dynamics of liquids confined between laterally heterogeneous interfaces. The heterogeneity can be related to topography (roughness), surface functionalisation (hydrophilic vs. hydrophobic), or surface charge (Fig. 11). One of the motivations is to understand the arrangement and mobility of ions in microporous materials composed of hydrophilic and hydrophobic moieties. Thus, smaller horizontal beam sizes will open up new experimental possibilities to answer these kind of scientific questions.

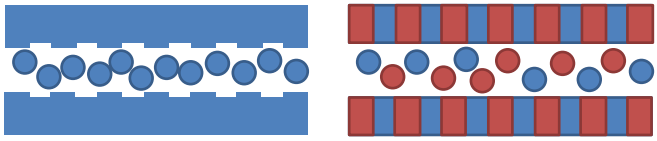

FIG. 11. (Color) Smaller vertical beam sizes available at upcoming diffraction limited storage rings will enable spatially resolved experiments on lateral inhomogeneous slit-pores. Examples include engineered surface topographies mimicking roughness (left) and hydrophilic vs. hydrophobic or negative vs. positive charged surface patterns (right).

ACKNOWLEDGMENTS

The authors acknowledge the help of Thomas Buslaps (ESRF) at beamline ID31, Marie Ruat (ESRF) for the support on the CdTe Maxipix detector, Michael Kappl (MPI-P) for AFM measurements, and thank Harald Reichert (ESRF), Milena Lippmann (PETRA III), and Hans-Jürgen Butt (MPI-P) for helpful discussions. J. M. and M. M. acknowledge the MAINZ Graduate School of Excellence, funded through the Excellence Initiative (DFG/GSC 266). M. V. was supported by an ERC Starting Grant (Grant No. 677663) and H. L. by the China Scholarship Council.

REFERENCES

[1] J. Zheng and T. Jow, J. Power Sources **62**, 155 (1996).
[2] P. Simon and Y. Gogotsi, Nat. Mater. **7**, 845 (2008).
[3] A. A. Lee, S. Kondrat, G. Oshanin, and A. A. Kornyshev, Nanotechnology **25** (2014).
[4] C. Largeot, C. Portet, J. Chmiola, P.-L. Taberna, Y. Gogotsi, and P. Simon, J. Am. Chem. Soc. **130** (2008).
[5] K. Kristiansen, M. Valtiner, G. W. Greene, J. R. Boles, and J. N. Israelachvili, Geochim. Cosmochim. Acta **75**, 6882 (2011).
[6] A. Riisager, P. Wasserscheid, R. van Hal, and R. Fehrmann, J. Catal. **219**, 452 (2003).
[7] T. Zemb, M. Klossek, T. Lopian, J. Marcus, S. Schöttl, D. Horinek, S. Prevost, D. Touraud, O. Diat, S. Marcelja, and W. Kunz, Proc. Nat. Acad. Sci. USA **113**, 4260 (2016).
[8] M. Bier, J. Mars, H. Li, and M. Mezger, Phys. Rev. E. **96**, 022603 (2017).
[9] O. Holloczki, A. Berkessel, J. Mars, M. Mezger, A. Wiebe, S. Waldvogel, and B. Kirchner, ACS Catal. **7**, 1846 (2017).
[10] H. Weiss, J. Mars, H. Li, G. Kircher, O. Ivanova, A. Feoktystov, O. Soltwedel, M. Bier, and M. Mezger, J. Phys. Chem. B (2016).
[11] J. Klein and E. Kumacheva, Science **269** (1995).
[12] A. L. Demirel and S. Granick, Phys. Rev. Lett. **77**, 2261 (1996).
[13] J. N. Israelachvili, P. M. Mcguiggan, and A. M. Homola, Science **240** (1988).

[14]H. Reichert, O. Klein, H. Dosch, M. Donk, *et al.*, Nature **408**, 839 (2000).
[15]M. Mezger, B. M. Ocko, H. Reichert, and M. Deutsch, Proc. Natl. Acad. Sci. USA **110**, 3733 (2013).
[16]B. Ocko, H. Hlaing, P. Jepsen, S. Kewalramani, A. Tkachenko, D. Pontoni, H. Reichert, and M. Deutsch, Phys. Rev. Lett. **106**, 137801 (2011).
[17]J. Mars, B. Hou, H. Weiss, H. Li, O. Konovalov, S. Festersen, B. M. Murphy, U. Rütt, M. Bier, and M. Mezger, Phys. Chem. Chem. Phys. **19**, 26651 (2017).
[18]W. J. Huisman, J. F. Peters, M. J. Zwanenburg, S. A. de Vries, T. E. Derry, D. Abernathy, and J. F. van der Veen, Nature **390**, 379 (1997).
[19]M. Mezger, H. Schröder, H. Reichert, J. S. O. Sebastian Schramm, S. Schöder, V. Honkimäki, M. Deutsch, B. M. Ocko, J. Ralston, M. Rohwerder, M. Stratmann, and H. Dosch, Science **322**, 424 (2008).
[20]L. Tamam, D. Pontoni, T. Hofmann, B. M. Ocko, H. Reichert, and M. Deutsch, J. Phys. Chem. Lett. **1**, 1041 (2010).
[21]M. Valtiner, X. Banquy, K. Kristiansen, G. W. Greene, and J. N. Israelachvili, Langmuir **28**, 13080 (2012).
[22]H.-W. Cheng, H. Weiss, P. Stock, Y.-J. Chen, C. R. Reinecke, J.-N. Dienemann, M. Mezger, and M. Valtiner, Langmuir **34**, 2637 (2018).
[23]M. Kind, W. Peukert, H. Rehage, and H. P. Schuchmann, *Colloid process engineering* (Springer, 2015).
[24]H. Li, M. Bier, J. Mars, H. Weiss, A.-C. Dippel, O. Gutowski, V. Honkimäki, and M. Mezger, Phys. Chem. Chem. Phys. **21**, 3734 (2019).
[25]K. Sentker, A. W. Zantop, M. Lippmann, T. Hofmann, O. H. Seeck, A. V. Kityk, A. Yildirim, A. Schönhals, M. G. Mazza, and P. Huber, Phys. Rev. Lett. **120**, 067801 (2018).
[26]Y. Golan, A. Martin-Herranz, Y. Li, C. R. Safinya, and J. Israelachvili, Phys. Rev. Lett. **86**, 1263 (2001).
[27]M. Ruths, S. Steinberg, and J. N. Israelachvili, Langmuir **12**, 6637 (1996).
[28]M. Lohmeier and E. Vlieg, J. Appl. Crystallogr. **26**, 706 (1993).
[29]J. Israelachvili, J. Colloid Interface Sci. **44**, 259 (1973).
[30]M. Schoen, C. L. Rhykerd Jr, D. J. Diestler, and J. H. Cushman, Science **245**, 1223 (1989).
[31]S. Granick, Science **253**, 1374 (1991).
[32]C. G. Schroer, I. Agapov, W. Brefeld, R. Brinkmann, Y.-C. Chae, H.-C. Chao, M. Eriksson, J. Keil, X. Nuel Gavaldà, R. Röhlsberger, O. H. Seeck, M. Sprung, M. Tischer, R. Wanzenberg, and E. Weckert, J. Synchrotron Rad. **25**, 1277 (2018).
[33]P. Raimondi, D. Einfeld, L. Farvacque, G. Le Bec, J.-C. Biasci, J.-F. Bouteille, J. Jacob, K. Scheidt, J. Chavanne, T. Perron, S. White, M. Hahn, and D. Martin, *EBS Storage Ring Technical Report* (ESRF - The European Synchrotron, 2018).
[34]J. Israelachvili, Y. Min, M. Akbulut, A. Alig, G. Carver, W. Greene, K. Kristiansen, E. Meyer, N. Pesika, K. Rosenberg, and H. Zeng, Rep. Prog. Phys. **73** (2010).
[35]M. Kittelmann, P. Rahe, and A. Kühnle, J. Phys.: Condens. Matter **24**, 354007 (2012).
[36]S. Kuhn and P. Rahe, Phys. Rev. B **89**, 235417 (2014).
[37]C. Marutschke, D. Walters, J. Cleveland, I. Hermes, R. Bechstein, and A. Kühnle, Nanotechnology **25**, 335703 (2014).
[38]H. Söngen, C. Marutschke, P. Spijker, E. Holmgren, I. M. Hermes, R. Bechstein, S. Klassen, J. Tracey, A. S. Foster, and A. Kühnle, Langmuir (2016).
[39]O. H. Seeck and B. Murphy, *X-ray Diffraction: Modern Experimental Techniques* (Pan Stanford, 2015).
[40]P. Willmott, *An introduction to synchrotron radiation: techniques and applications* (John Wiley & Sons, 2011).
[41]T. A. Ezquerra, M. C. Garcia-Gutierrez, A. Nogales, and M. Gomez, *Applications of synchrotron light to scattering and diffraction in materials and life sciences*, Vol. 776 (Springer, 2009).
[42]B. Ocko, J. Wang, A. Davenport, and H. Isaacs, Phys. Rev. Lett. **65**, 1466 (1990).
[43]P. Reichert, K. S. Kjær, T. B. van Driel, J. Mars, J. W. Ochsmann, D. Pontoni, M. Deutsch, M. M. Nielsen, and M. Mezger, Faraday Discussions (2017).
[44]F. Perakis, G. Camisasca, T. J. Lane, A. Späh, K. T. Wikfeldt, J. A. Sellberg, F. Lehmkühler, H. Pathak, K. H. Kim, K. Amann-Winkel, *et al.*, Nature comm. **9**, 1917 (2018).
[45]M. P. Olbinado, V. Cantelli, O. Mathon, S. Pascarelli, J. Grenzer, A. Pelka, M. Roedel, I. Prencipe, A. L. Garcia, U. Helbig, *et al.*, Journal of Physics D: Applied Physics **51**, 055601 (2018).
[46]S. Całus, B. Jabłońska, M. Busch, D. Rau, P. Huber, and A. V. Kityk, Phys. Rev. E **89**, 062501 (2014).
[47]S. Całus, M. Busch, A. V. Kityk, W. Piecek, and P. Huber, J. Phys. Chem. C **120**, 11727 (2016).
[48]A. V. Kityk and P. Huber, Appl. Phys. Lett. **97**, 153124 (2010).
[49]Y. Suzuki, H. Duran, M. Steinhart, H.-J. Butt, and G. Floudas, Soft Matter **9**, 2621 (2013).
[50]Y. Yao, T. Sakai, M. Steinhart, H.-J. Butt, and G. Floudas, Macromolecules **49**, 5945 (2016).
[51]W. Lee, K. Schwirn, M. Steinhart, E. Pippel, R. Scholz, and U. Gösele, Nat. Nanotechnology **3**, 234 (2008).
[52]K. Schwirn, W. Lee, R. Hillebrand, M. Steinhart, K. Nielsch, and U. Gösele, ACS Nano **2**, 302 (2008).
[53]L. Zhao, M. Yosef, M. Steinhart, P. Göring, H. Hofmeister, U. Gösele, and S. Schlecht, Angew. Chem. Int. Ed. **45**, 311 (2006).
[54]P. Huber, J. Phys.: Condens. Matter **27**, 103102 (2015).
[55]B. Lindlar, A. Kogelbauer, P. J. Kooyman, and R. Prins, Microporous Mesoporous Mater. **44**, 89 (2001).
[56]A. Yildirim, K. Sentker, G. J. Smales, B. R. Pauw, P. Huber, and A. Schönhals, Nanoscale Advances **1**, 1104 (2019).
[57]Y. Suzuki, H. Duran, W. Akram, M. Steinhart, G. Floudas, and H.-J. Butt, Soft Matter **9**, 9189 (2013).
[58]C. Franz, F. Lange, Y. Golitsyn, B. Hartmann-Azanza, M. Steinhart, M. Krutyeva, and K. Saalwächter, Macromolecules **49**, 244 (2016), https://doi.org/10.1021/acs.macromol.5b02309.
[59]M. Ndao, R. Lefort, C. Cerclier, R. Busselez, D. Morineau, B. Frick, J. Ollivier, A. V. Kityk, and P. Huber, Royal Society of Chemistry Advances **4**, 59358 (2014).
[60]J. J. Thomson, *Applications of dynamics to physics and chemistry* (Macmillan, 1888).
[61]F. Meissner, Z. anorg. allg. Chem. **110**, 169 (1920).
[62]E. Rie, Z. phys. Chem. **104**, 354 (1923).
[63]H. Hansen-Goos and J. Wettlaufer, Phys. Rev. E **81**, 031604 (2010).
[64]S. H. Idziak, C. R. Safinya, R. S. Hill, K. E. Kraiser, M. Ruths, H. E. Warriner, S. Steinberg, K. S. Liang, J. N. Israelachvili, *et al.*, Science , 1915 (1994).
[65]S. Idziak, I. Koltover, K. Liang, J. Israelachvili, and C. Safinya, Int. J. Thermophys. **16**, 299 (1995).
[66]S. H. Idziak, I. Koltover, J. N. Israelachvili, and C. R. Safinya, Phys. Rev. Lett. **76**, 1477 (1996).
[67]I. Koltover, S. Idziak, P. Davidson, Y. Li, C. Safinya, M. Ruths, S. Steinberg, and J. Israelachvili, J. Physique II **6**, 893 (1996).
[68]Y. Li, Y. Golan, A. Martin-Herranz, O. Pelletier, M. Yasa, J. Israelachivili, and C. Safinya, Int. J. Thermophys. **22**, 1175 (2001).
[69]Y. Golan, M. Seitz, C. Luo, A. Martin-Herranz, M. Yasa, Y. Li, C. R. Safinya, and J. Israelachvili, Rev. Sci. Instrum. **73**, 2486 (2002).
[70]T. Becker, *Collapse dynamics of confined liquid films*, Ph.D. thesis, University of Twente (2005).
[71]K. Nygård, R. Kjellander, S. Sarman, S. Chodankar, E. Perret, J. Buitenhuis, and J. Van der Veen, Phys. Rev. Lett. **108**, 037802 (2012).
[72]E. Perret, K. Nygård, D. K. Satapathy, T. Balmer, O. Bunk, M. Heuberger, and J. van der Veen, EPL **88**, 36004 (2009).
[73]E. Perret, *Structure of molecular liquids under nanometre confinement*, Ph.D. thesis, ETH Zürich (2010).

[74]E. Perret, K. Nygård, D. K. Satapathy, T. E. Balmer, O. Bunk, M. Heuberger, and J. F. van der Veen, J. Phys.: Condens. Matter **22**, 235102 (2010).
[75]E. Perret, K. Nygård, D. K. Satapathy, T. E. Balmer, O. Bunk, M. Heuberger, and J. F. van der Veen, J. Synchrotron Radiat. **17**, 465 (2010).
[76]O. H. Seeck, H. Kim, D. R. Lee, D. Shu, I. D. Kaendler, J. K. Basu, and S. K. Sinha, EPL **60**, 376 (2002).
[77]M. Lippmann, A. Ehnes, and O. Seeck, Rev. Sci. Instrum. **85**, 015106 (2014).
[78]M. Lippmann, O. H. Seeck, A. Ehnes, K. Nygard, F. Bertram, and A. Ciobanu, J. Phys. Chem. Lett. **10**, 1634 (2019).
[79]K. Tomita, M. Mizukami, S. Nakano, N. Ohta, N. Yagi, and K. Kurihara, Phys. Chem. Chem. Phys. (2018).
[80]T. Kuhl, G. Smith, J. Majewski, W. Hamilton, and N. Alcantar, Neutron News **14**, 29 (2003).
[81]T. L. Kuhl, G. S. Smith, J. N. Israelachvili, J. Majewski, and W. Hamilton, Rev. Sci. Instrum. **72**, 1715 (2001).
[82]W. Hamilton, G. Smith, N. Alcantar, J. Majewski, R. Toomey, and T. Kuhl, Journal of Polymer Science Part B: Polymer Physics **42**, 3290 (2004).
[83]W. M. de Vos, L. L. E. Mears, R. M. Richardson, T. Cosgrove, R. M. Dalgliesh, and S. W. Prescott, Rev. Sci. Instrum. **83** (2012), 10.1063/1.4767238.
[84]S. B. Abbott, W. M. de Vos, L. L. E. Mears, B. Cattoz, M. W. A. Skoda, R. Barker, R. M. Richardson, and S. W. Prescott, Macromolecules **48**, 2224 (2015).
[85]W. M. de Vos, L. L. E. Mears, R. M. Richardson, T. Cosgrove, R. Barker, and S. W. Prescott, Macromolecules **46**, 1027 (2013).
[86]Z. Wei and S. W. Prescott, Curr. Opin. Colloid Interface Sci. **20**, 253 (2015).
[87]L. L. E. Mears, *Adsorption and Confinement Effects in Liquid Crystals*, Phd thesis, University of Bristol (2015).
[88]M. Wolff, B. Akgun, M. Walz, A. Magerl, and H. Zabel, EPL **82**, 36001 (2008).
[89]M. Wolff, P. Gutfreund, A. Rühm, B. Akgun, and H. Zabel, J. Phys.: Condens. Matter **23**, 184102 (2011).
[90]M. Wolff, P. Kuhns, G. Liesche, J. F. Ankner, J. F. Browning, and P. Gutfreund, J. Appl. Crystallogr. **46**, 1729 (2013).
[91]F. Schwoerer, M. Trapp, M. Ballauff, R. Dahint, and R. Steitz, Langmuir **31**, 11539 (2015).
[92]B. Struth, K. Hyun, E. Kats, T. Meins, M. Walther, M. Wilhelm, and G. Grübel, Langmuir **27**, 2880 (2011).
[93]R. Miller, J. K. Ferri, A. Javadi, J. Krägel, N. Mucic, and R. Wüstneck, Colloid Polym. Sci. **288**, 937 (2010).
[94]N. Mucic, A. Javadi, N. Kovalchuk, E. Aksenenko, and R. Miller, Adv. Colloid Interface Sci. **168**, 167 (2011).
[95]D. Stamou, D. Gourdon, M. Liley, N. A. Burnham, A. Kulik, H. Vogel, and C. Duschl, Langmuir **13**, 2425 (1997).
[96]M. Liley, T. A. Keller, C. Duschl, and H. Vogel, Langmuir **13**, 4190 (1997).
[97]B. Song, W. Walczyk, and H. Schönherr, Langmuir **27**, 8223 (2011).
[98]N. Vogel, J. Zieleniecki, and I. Köper, Nanoscale **4**, 3820 (2012).
[99]W. J. Huisman, J. Peters, J. Derks, H. Ficke, D. Abernathy, and J. Van Der Veen, Rev. Sci. Instrum. **68**, 4169 (1997).
[100]H. Reichert, V. Honkimäki, A. Snigirev, S. Engemann, and H. Dosch, Physica B: Condensed Matter **336**, 46 (2003).
[101]V. Honkimäki, H. Reichert, J. Okasinski, and H. Dosch, J. Synchrotron Radiat. **13**, 426 (2006).
[102]A. A. Snigirev, B. Filseth, P. Elleaume, T. Klocke, V. Kohn, B. Lengeler, I. Snigireva, A. Souvorov, and J. Tuemmler, in *Optical Science, Engineering and Instrumentation'97* (International Society for Optics and Photonics, 1997) pp. 164–170.
[103]A. Snigirev, I. Snigireva, G. Vaughan, J. Wright, M. Rossat, A. Bytchkov, and C. Curfs, J. Phys. Conf. Ser. **186**, 012073 (2009).
[104]M. Hoskin, J. Hist. Astron. **38**, 487 (2007).
[105]S. Nakano, M. Mizukami, and K. Kurihara, Soft matter **10**, 2110 (2014).
[106]S. Nakano, M. Mizukami, N. Ohta, N. Yagi, I. Hatta, and K. Kurihara, Jpn. J. Appl. Phys. **52** (2013).
[107]C. Safinya, E. Sirota, and R. Plano, Phys. Rev. Lett. **66**, 1986 (1991).
[108]W. H. De Jeu, *Basic X-ray scattering for soft matter* (Oxford University Press, 2016).
[109]J. W. Goodby, P. J. Collings, T. Kato, C. Tschierske, H. F. Gleeson, and P. Raynes, *Handbook of liquid crystals* (Wiley-Vch, 2014).
[110]B. Mukherjee, C. Peter, and K. Kremer, Physical Review E **88**, 010502 (2013).
[111]D. Lis, E. H. G. Backus, J. Hunger, S. H. Parekh, and M. Bonn, Science **344**, 1138 (2014), https://science.sciencemag.org/content/344/6188/1138.full.pdf.
[112]G. Krämer, F. Hausen, and R. Bennewitz, Faraday Discuss. **199**, 299 (2017).
[113]S. Schöttl and D. Horinek, Curr. Op. Coll. Inter. Sci. **22**, 8 (2016).
[114]M. Mezger, R. Roth, H. Schröder, P. Reichert, D. Pontoni, and H. Reichert, J. Chem. Phys. **142**, 164707 (2015).
[115]Z. Brkljaca, M. Klimczak, Z. Milicevic, M. Weisser, N. Taccardi, P. Wasserscheid, D. M. Smith, A. Magerl, and A. S. Smith, J. Phys. Chem. Lett. **6**, 549 (2015).
[116]E. Sloutskin, B. M. Ocko, L. Tamam, I. Kuzmenko, T. Gog, and M. Deutsch, J. Am. Chem. Soc. **127**, 7796 (2005).
[117]J. Haddad, D. Pontoni, B. M. Murphy, S. Festersen, B. Runge, O. M. Magnussen, H.-G. Steinrück, H. Reichert, B. M. Ocko, and M. Deutsch, Proc. Natl. Acad. Sci. U.S.A. , 201716418 (2018).
[118]H. K. Kashyap, J. J. Hettige, H. V. Annapureddy, and C. J. Margulis, Chem. Commun. **48**, 5103 (2012).
[119]S. W. Coles, A. M. Smith, M. V. Fedorov, F. Hausenaef, and S. Perkin, Faraday Discuss. **206**, 427 (2018).
[120]R. Atkin and G. Warr, J. Phys. Chem. C **111**, 5162 (2007).

BIOGRAPHY

Markus Mezger is group leader at the Max-Planck-Institute for Polymer Research (MPI-P) and assistant professor at the Institute of Physics, Johannes Gutenberg University Mainz, Germany. He received his PhD in physics in 2008 from the University of Stuttgart. After postdoctoral research at the Department of Chemical Engineering, University of California, Berkeley, and at Lawrence Berkeley National Lab, he joined MPI-P in 2010. His scientific interest focuses on the structure and dynamics of soft matter at interfaces and in confinement studied by X-ray and neutron scattering techniques. Current research topics address ionic liquids, electrolyte solutions, water, ice, and polymers.

Markus Valtiner is professor for applied interface physics at the Vienna University of Technology (TU Wien). He received his PhD in 2008 for his graduate work at the Max-Planck-Institute for Ironresearch (MPIE) in Düsseldorf, Germany. From 2009 to 2012 he worked as postdoctoral researcher at the Department of Chemical Engineering, University of California, Santa Barbara. In 2012 he again joined the MPIE as a group leader, and from 2016-2017 he was professor for physical chemistry at the Freiberg University of Technology. His scientific interest is focused on solid/liquid interfaces, single molecular interactions, adhesion as well as corrosion in confined spaces using force probe experiments and in particular the surfaces forces apparatus.

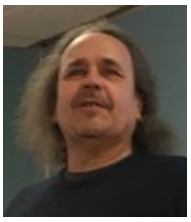

Veijo Honkimäki is the head of the Structure of Materials group at ESRF. He is also in charge of the High-Energy Beamline for Buried Interface Structure and and Materials processing, ID31.

Frank Uwe Renner Frank Uwe Renner is Professor for Energy Materials and Physics at the Institute for Materials Science of Hasselt University in Belgium, and the joint research center IMOMEC of Hasselt University and IMEC. After obtaining a doctorate from University of Stuttgart in Germany, he persued postdoctoral research at the European Synchrotron Radiation Facility in Grenoble, France, and with an Alexander-von-Humboldt stipend, at the Research Institute for Ubiquitous Energy Devices at AIST Ikeda in Japan. From 2007 to 2013 he was a research group leader at the Max-Planck-Institute for Iron Research in Düsseldorf, Germany. Frank Uwe Renner uses Synchrotron Light, and is involved in APT-Flanders and the installation of a lab-based HAX-PES setup at Hasselt University. His scientific interests center around surface science and electrochemistry including the mechanistic understanding of corrosion processes, Li-ion battery electrodes and interfaces, but also bio-related lipid membranes.

Henning Weiss received his PhD in the group of Markus Mezger in 2018 with the thesis entitled "Structure of Confined Liquids Studied by an X-Ray Surface Force Apparatus". Currently he is working as a IT consultant at Bilfinger.

Hsiu-Wei Cheng is university assistant in the group for applied interface physics at the Vienna University of Technology (TU Wien). He received his PhD from Ruhr University Bochum in 2017. Afterward he was post doctoral researcher at the Freiberg University of Technology.

Julian Mars is a PhD student in the group of Markus Mezger where he studies the structure of ionic liquids near liquid/vapour interfaces.

Hailong Li received his PhD in the group of Markus Mezger in 2017 with the thesis entitled "Interfacial Premelting of Ice in Nanocomposite Materials". Currently he is a postdoc in the Department of Fibre and Polymer Technology at KTH Royal Institute of Technology, Stockholm.

Claudia Merola received her PhD in the group of Markus Valtiner in 2019 with the thesis entitled "Unravelling the corrosion mechanism in nanometer confined gaps using white light interferometry in reflection and transmission mode".